

# Layered nanocomposites by shear-flow-induced alignment of nanosheets

<https://doi.org/10.1038/s41586-020-2161-8>

Received: 8 May 2018

Accepted: 24 January 2020

Published online: 8 April 2020

 Check for updates

Chuangqi Zhao<sup>1,7</sup>, Pengchao Zhang<sup>1,7</sup>, Jiajia Zhou<sup>1,2,7</sup>, Shuanhu Qi<sup>1,2</sup>, Yoshihiro Yamauchi<sup>3</sup>, Ruirui Shi<sup>1</sup>, Ruochen Fang<sup>1</sup>, Yasuhiro Ishida<sup>3</sup>, Shutao Wang<sup>4</sup>, Antoni P. Tomsia<sup>1,5</sup>, Lei Jiang<sup>1,4,5,6</sup> & Mingjie Liu<sup>1,2,5,6</sup>

Biological materials, such as bones, teeth and mollusc shells, are well known for their excellent strength, modulus and toughness<sup>1–3</sup>. Such properties are attributed to the elaborate layered microstructure of inorganic reinforcing nanofillers, especially two-dimensional nanosheets or nanoplatelets, within a ductile organic matrix<sup>4–6</sup>. Inspired by these biological structures, several assembly strategies—including layer-by-layer<sup>4,7,8</sup>, casting<sup>9,10</sup>, vacuum filtration<sup>11–13</sup> and use of magnetic fields<sup>14,15</sup>—have been used to develop layered nanocomposites. However, how to produce ultrastrong layered nanocomposites in a universal, viable and scalable manner remains an open issue. Here we present a strategy to produce nanocomposites with highly ordered layered structures using shear-flow-induced alignment of two-dimensional nanosheets at an immiscible hydrogel/oil interface. For example, nanocomposites based on nanosheets of graphene oxide and clay exhibit a tensile strength of up to  $1,215 \pm 80$  megapascals and a Young's modulus of  $198.8 \pm 6.5$  gigapascals, which are 9.0 and 2.8 times higher, respectively, than those of natural nacre (mother of pearl). When nanosheets of clay are used, the toughness of the resulting nanocomposite can reach  $36.7 \pm 3.0$  megajoules per cubic metre, which is 20.4 times higher than that of natural nacre; meanwhile, the tensile strength is  $1,195 \pm 60$  megapascals. Quantitative analysis indicates that the well aligned nanosheets form a critical interphase, and this results in the observed mechanical properties. We consider that our strategy, which could be readily extended to align a variety of two-dimensional nanofillers, could be applied to a wide range of structural composites and lead to the development of high-performance composites.

Liquid flow can facilitate the oriented assembly of nanofillers by controlling the advancing or receding motion of the three-phase contact line<sup>16–18</sup>. Recently, we observed that liquid droplets could rapidly and entirely spread on a miscible gel surface in an oil/water/gel system<sup>19–21</sup>, and we refer to this as superspreading. Our present results show that a droplet of reaction solution containing graphene oxide (GO) nanosheets and sodium alginate (NaAlg) can achieve superspreading within 358 ms on the surface of a fully swollen polyacrylamide (PAAm) hydrogel under silicone oil, resulting in a homogeneous liquid layer at the hydrogel/oil interface (Fig. 1a and Supplementary Fig. 1). By using an array of syringes to extrude the reaction solutions (see below for compositions) simultaneously, we extended the superspreading process to a continuous system to produce large-area nanocomposite films with aligned nanosheets (Fig. 1b).

In this study, a reaction solution containing well-dispersed GO nanosheets (Supplementary Fig. 2) and NaAlg (solution A in Fig. 1b) was used to demonstrate the utility of our superspreading layering

strategy. With appropriate choices of flow rate, distance between adjacent syringes and moving speed of hydrogel, the multiple sources of solution A from arrayed syringes rapidly spread and fused to form a uniform superspreading solution layer at the oil/hydrogel interface. Meanwhile, calcium ions ( $\text{Ca}^{2+}$ ) in the hydrogel, which was previously immersed in calcium chloride solution (solution B in Fig. 1b), diffused from the hydrogel surface into the superspreading layer of solution A. The  $\text{Ca}^{2+}$  ions created crosslinks of NaAlg, and consequently the superspreading layer containing GO nanosheets was converted into a calcium alginate (CA) hydrogel film within 3 min (see Methods). This CA hydrogel film could then be readily separated from the hydrogel surface after immersion in a water bath. After the gel was dried, we collected continuous and uniform GO/CA nanocomposite films without defects as a roll, in this instance about 5 cm in width, with clear opportunities for scaling up (Fig. 1b).

The superspreading process provides a strong shear flow force, which is highly desirable for achieving in-plane stacked 2D nanosheets<sup>22</sup>.

<sup>1</sup>Key Laboratory of Bioinspired Smart Interfacial Science and Technology of Ministry of Education, School of Chemistry, Beihang University, Beijing, China. <sup>2</sup>International Research Institute for Multidisciplinary Science, Beihang University, Beijing, China. <sup>3</sup>RIKEN Center for Emergent Matter Science, Wako, Japan. <sup>4</sup>CAS Key Laboratory of Bio-Inspired Materials and Interfacial Science, CAS Center for Excellence in Nanoscience, Technical Institute of Physics and Chemistry, Chinese Academy of Sciences, Beijing, China. <sup>5</sup>Beijing Advanced Innovation Center for Biomedical Engineering, Beihang University, Beijing, China. <sup>6</sup>Research Institute of Frontier Science, Beihang University, Beijing, China. <sup>7</sup>These authors contributed equally: Chuangqi Zhao, Pengchao Zhang, Jiajia Zhou.  e-mail: liumj@buaa.edu.cn

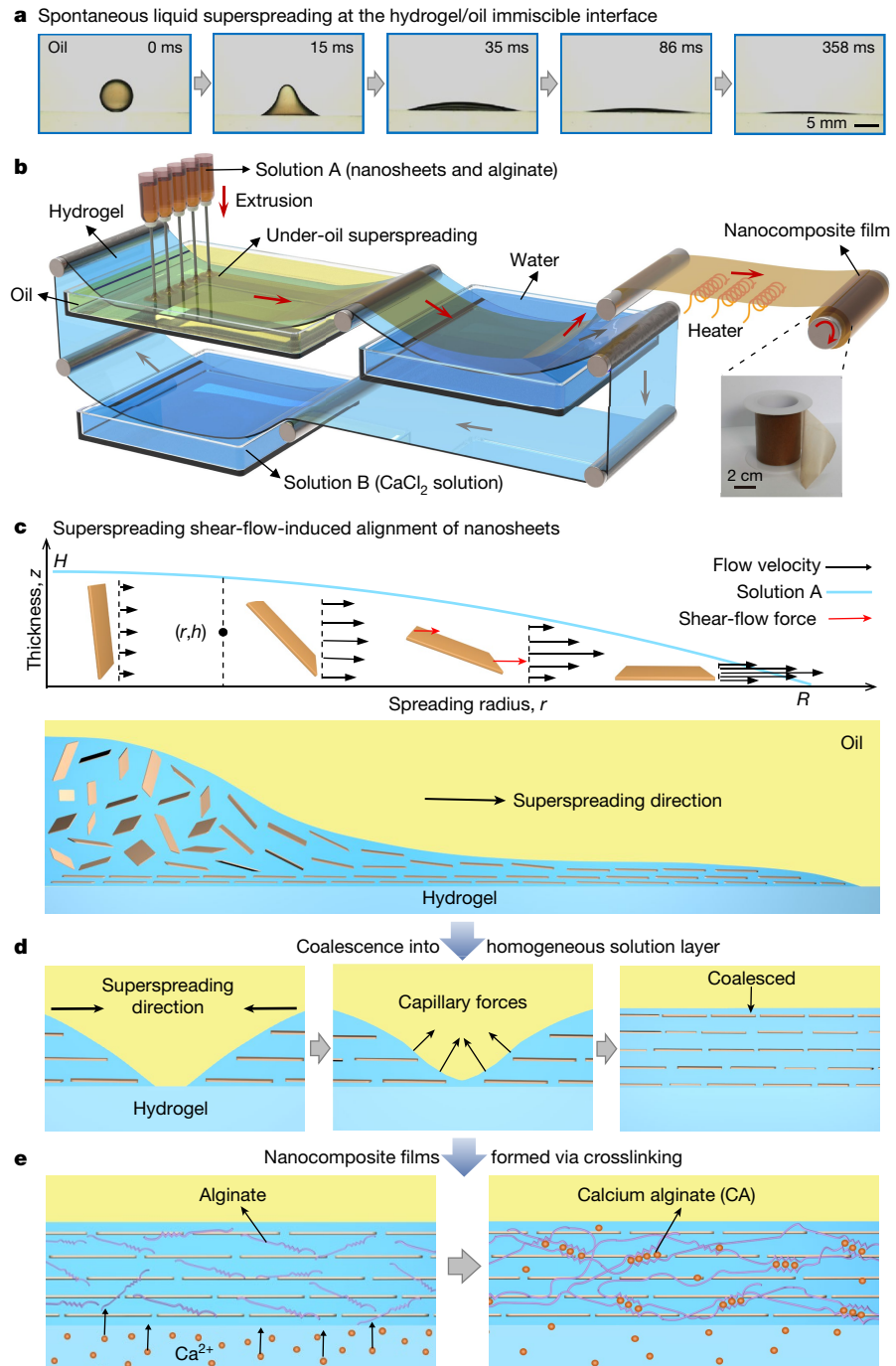


**Fig. 1 | Fabrication and mechanism of the layered nanocomposite films featuring aligned nanosheets.** **a**, A solution droplet (10  $\mu\text{l}$ ) achieves spontaneous and complete spreading at the hydrogel/oil interface, forming a thin spreading solution layer. The composition of the reaction solution is 0.09 wt% GO and 0.18 wt% NaAlg. **b**, Schematic of the continuous fabrication of large-area nanocomposite films, with steps involving superspreading under oil, crosslinking NaAlg by calcium ( $\text{Ca}^{2+}$ ) ions, separating the gel films from the hydrogel surface, drying and collecting. Inset, a roll of the prepared large-area

nanocomposite film. The reaction solution A contains nanosheets and NaAlg. The solution B contains  $\text{CaCl}_2$ . **c**, The theoretical study (top panel) and schematic (bottom panel) of the mechanism of shear-flow-induced alignment of nanosheets in the superspreading process.  $R$  and  $H$  are the radius and height of the droplet, respectively. **d**, The edges of the layers of spreading solution A from two adjacent syringes coalesce by capillary force into a continuous and uniform liquid layer. **e**, The aligned nanosheets were fixed by in situ crosslinking of NaAlg with  $\text{Ca}^{2+}$  ions.

To understand shear-flow-induced alignment during the superspreading process, we analysed the velocity inside the spreading liquid,  $v(r, z; t)$  (where  $r-z$  are the cylindrical coordinates and  $t$  is time; see Fig. 1c). The boundary condition at the substrate was  $v(r, z=0; t)=0$ . Near the interface, we assume a no-slip boundary condition because the viscosity of the surrounding fluid is much larger than that of the liquid

droplet. The resulting height-averaged flow velocity  $\bar{v}(r)$  can be described by the following equation:

$$\bar{v}(r) = \frac{1}{h} \int_0^h v(r, z) dz = \frac{1}{6} h^2 A = r \frac{\dot{R}}{R}$$

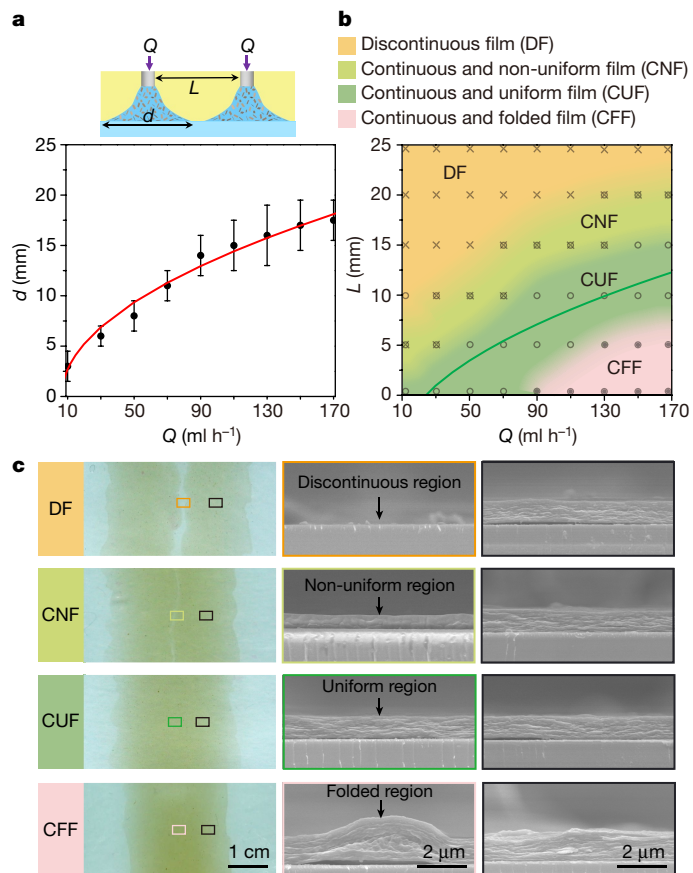


**Fig. 2 | Control over the uniformity and continuity of the layered nanocomposite films.** **a**, Main panel, the measured value of spreading diameter  $d$  as a function of flow rate  $Q$  can be fitted well by  $d \propto Q^{1/2}$  (red line), for a given reaction solution with a viscosity of 6 mPa s. The moving speed of the hydrogel substrate was 5 mm s<sup>-1</sup>. Error bars, ±1 s.d. Top, sketch showing variables. **b**, The state diagram of the effect of flow rate  $Q$  and distance  $L$  between two adjacent syringes on the uniformity and continuity of the layered nanocomposite films. The optimal separation is  $L = d(Q) - 6$  mm (green line). **c**, Four kinds of nanocomposite films formed as a function of distance  $L$ , including the discontinuous film (DF), continuous but non-uniform film (CNF), continuous and uniform film (CUF), and continuous and folded film (CFF). Leftmost column, optical images showing areas examined by scanning electron microscopy (SEM). The SEM images featuring a colour border (central column) and a black border (rightmost column) were taken from the coalescence region of two adjacent syringes and the section below the nozzle of the syringe, respectively.

in which  $A$  is a function of  $r$ ,  $h$  is the height at position  $r$  and  $\dot{R} = dR/dt$  is the velocity of the contact line (see Methods and Extended Data Figs. 1 and 2). The results of these analyses show that the velocity  $v$  and the shear rate  $\partial v/\partial z$  are higher near the contact line than near the centre of the spreading solution. Thus, the superspreading process results in an efficient shear flow force, which is responsible for the alignment of 2D nanosheets (Fig. 1c). As the edges of the superspreading layers from two adjacent syringes draw near each other, they coalesce under capillary force, leading to the formation of a homogeneous superspreading layer (Fig. 1d). Subsequently, the transiently aligned nanosheets are rapidly fixed via in situ Ca<sup>2+</sup>-induced crosslinking of NaAlg (Fig. 1e), forming layered nanocomposite films (Supplementary Figs. 3 and 4).

The spreading diameter  $d$  of the reaction solution from a single syringe and distance  $L$  between two adjacent syringes are crucial for the continuous fabrication of uniform nanocomposite films (Fig. 2). We first determined the spreading diameter  $d$  from a single syringe when

the reaction solution completed the superspreading process (Fig. 2a);  $d$  increased along with the increase of the flow rate  $Q$ . The quantitative analysis indicates the relationship between  $d$  and  $Q$  as  $d \propto Q^{1/2}$  (Fig. 2a, Methods). Additionally, a larger spreading diameter can be obtained by reducing the moving speed of the hydrogel substrate or the solution viscosity (see Methods and Extended Data Fig. 3). Then, the distance  $L$  between two adjacent syringes must be chosen carefully to realize the continuity and uniformity of the prepared nanocomposite films. When the  $L$  was slightly less than the  $d$ , continuous but non-uniform films were obtained owing to the lack of spreading force at the edge of the spreading solution layers, preventing them from coalescing. Assuming the levelling is driven by capillary force, we estimated that the distance needed to be in the range  $d > L > d - 8$  mm in order to obtain a continuous and uniform film (see Methods). Our experimental results show the optimal separation between two adjacent syringes is  $L = d(Q) - 6$  mm (Fig. 2b, c), which agrees with the theoretical analysis. Furthermore, when keeping the distance  $L$  constant, continuous and uniform films could also be prepared by increasing the flow rate  $Q$  (Supplementary Fig. 5). Nanocomposite films with controlled thickness, ranging from approximately 600 nm to 1,400 nm, could be prepared by adjusting the concentration of GO nanosheets in the superspreading solutions (Supplementary Fig. 6).

The highly aligned GO nanosheets were then systematically characterized using transmission electron microscopy (TEM) and small-angle X-ray scattering (SAXS)<sup>23</sup>. As shown in Fig. 3a, TEM images of the cross-section reveal the aligned nature of the GO nanosheets in the GO/CA nanocomposite films prepared by the superspreading method (abbreviated as SS-GO/CA). In contrast, the nanocomposite films made by a partial spreading process (abbreviated as PS-GO/CA; Supplementary Fig. 7) have randomly distributed and severely intertwined GO nanosheets (Fig. 3b). The orientation degree of the GO nanosheets was further quantitatively evaluated by SAXS analysis. The 2D SAXS pattern of the SS-GO/CA nanocomposite films shows two strong diffuse spots in the equatorial direction. The corresponding azimuthal angle ( $\varphi$ ) plot features two sharp peaks at  $\varphi = 90^\circ$  and  $270^\circ$ . The calculated orientation order parameter ( $f$ ) is as high as 0.89, indicating that the GO nanosheets are well-assembled (Fig. 3a). In contrast, the PS-GO/CA nanocomposite films show an isotropic scattering pattern, a nearly flat  $\varphi$  plot and a small  $f(0.02)$ ; Fig. 3b), indicating the random distribution of GO nanosheets. Moreover, we also fabricated the layered nanocomposite films with different weight percentages of GO nanosheets (2, 8, 15 and 33 wt%) using the superspreading strategy. The corresponding TEM and SAXS images show a highly ordered assembly of GO nanosheets in all the nanocomposite films (Fig. 3c, d and Supplementary Fig. 8). These results suggest that our superspreading layering strategy can achieve rapid assembly of nanosheets and fixation of the ordered structures by using dilute reaction solutions, thus preventing possible aggregation of nanofillers during the fabrication processes<sup>24–26</sup>.

Furthermore, this superspreading strategy can be extended to other 2D nanofillers, such as clay nanosheets (Supplementary Fig. 9). The orientation order parameter  $f$  of the resulting clay/CA nanocomposite films can be as high as 0.82 (Supplementary Fig. 10). Importantly, this superspreading strategy is generalizable and scalable. We achieved the fabrication of nanocomposite films by using thermal and photo-initiated polymerization of other covalent and non-covalent polymers, such as agarose and acrylamides systems (Supplementary Fig. 11), among many others. This technique opens an avenue for the continuous fabrication of layered nanocomposite films with highly ordered assembled nanosheets in a universal and efficient way.

By using these highly aligned nanosheets, we have successfully achieved one-step fabrication of large-area ultra-strong layered nanocomposite films. Polyvinyl alcohol (PVA) and single-wall carbon nanotubes (CNTs) were introduced into the reaction solutions because of their enhanced interactions with nanosheets via hydrogen bonds and van der Waals forces<sup>10,27,28</sup>. The low viscosities of the resulting

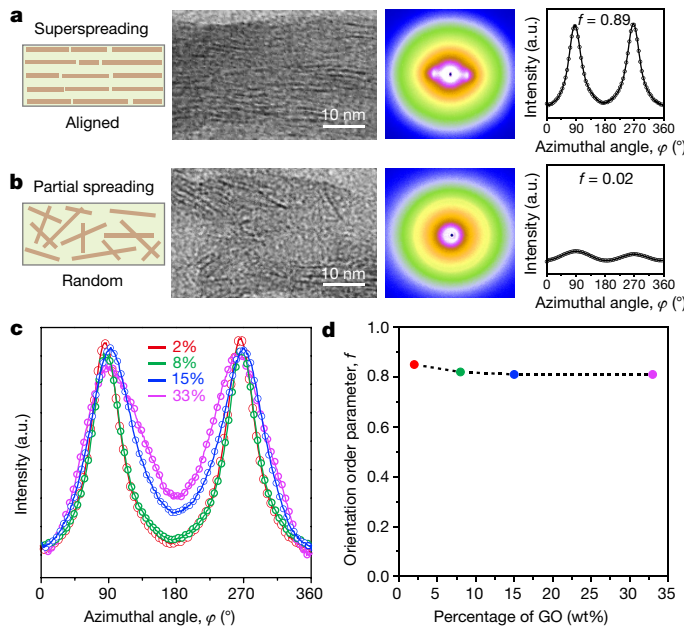


**Fig. 3 | Structural characterization of the layered nanocomposite films.**

**a, b,** Left to right: schematics, TEM images, 2D SAXS images and azimuthal angle ( $\varphi$ ) plots of the GO/CA nanocomposite films prepared via superspreading (a) and partial spreading (b) methods. **c, d,** Plots of  $\varphi$  (c) and the orientation order parameter ( $f$ ; d) of the layered nanocomposite films with four different weight percentages of GO nanosheets prepared by the superspreading strategy. These results confirmed that GO nanosheets were assembled into highly ordered structures in all these films.

reaction solutions (4–7 mPa s) (Supplementary Tables 1 and 2) enable the realization of the superspreading process and minimize the possible aggregation of nanofillers (Supplementary Table 3 and Supplementary Video 1). Importantly, the utilization of multiple reinforcing nanosheets can synergistically improve the mechanical performance of nanocomposite films<sup>29–32</sup>. By optimizing the weight percentage of the nanofillers (GO, clay and CNTs), we obtained nanocomposite films (abbreviated as SS-GO/clay/CNT) with the highest known tensile strength ( $1,215 \pm 80$  MPa) and modulus ( $198.8 \pm 6.5$  GPa) (Fig. 4a, Supplementary Figs. 12–14, Supplementary Tables 4–7, and Extended Data Table 1). In contrast, keeping the same ratio of nanofillers to polymers, a higher concentration of the reaction solutions leads to markedly decreased mechanical performance because of the aggregation of nanofillers and the decrease of orientation order parameter (Supplementary Fig. 15, Extended Data Fig. 4, and Supplementary Tables 5 and 6). Characterization of the orientation degree of the assembled nanosheets indicates that the weight percentage of nanofillers is also important for the high mechanical performance of the SS-GO/clay/CNT nanocomposite films—in addition to the above-mentioned well-dispersed and highly ordered structure of the nanofillers (Extended Data Fig. 5 and Supplementary Fig. 16).

To elucidate the underlying mechanism, we measured the interlayer distance of nanosheets in nanocomposite films with different weight percentages of nanofillers. As shown in Fig. 4b and Extended Data Table 1, the interlayer distance decreases as the weight percentage of nanofillers increases. When the interlayer distance reaches about 2.6 nm, the SS-GO/clay/CNT nanocomposite films show the best mechanical performance (Extended Data Table 1). Further decreasing the interlayer distance leads to a slight decrease of the mechanical properties. We further explored if the change of interlayer distance could alter the mobility of polymer chains, which could greatly influence the interfacial interaction between polymers and nanosheets. The strong shift in glass transition temperature ( $T_g$ ) towards the higher values (Fig. 4c and Supplementary Fig. 17) confirms the suppression of

the thermal motion of the polymer chains when they were constrained between aligned nanosheets.

On the basis of these experimental results, we conclude that the formation of a critical interphase by the well-aligned nanosheets was essential to the ultra-strong mechanical properties (Fig. 4d). The good dispersion and high alignment of nanosheets and strong interactions with matrix polymers (Supplementary Fig. 18) lead to the formation of an interphase around each nanosheet in which the mobility of the matrix polymer chains is decreased<sup>4,32–34</sup>. When the weight percentage of nanofillers is low, the interlayer distance  $d$  is larger than the critical interlayer distance  $d_c$ . Free polymer chains are present abundantly between the nanofillers, leading to the formation of a discrete interphase (blue) within a continuous bulk matrix (light blue) and consequently low mechanical properties (I in Fig. 4d). Increasing the weight percentage of nanofillers induces the interlayer distance down to the critical value, resulting in the formation of a critical interphase (II in Fig. 4d). Within such a critical interphase, the polymer chains were effectively stiffened under strong confinement, and their mobility was reduced owing to extensive interactions with the nanosheets, which was verified by the shift of  $T_g$  towards higher values. Further increasing the weight percentage of nanofillers induces the further suppression of the thermal motion of polymer chains, leading to an ill-defined  $T_g$  as no obvious  $\tan\delta$  peaks (Fig. 4c) can be observed<sup>4</sup>. However, the high weight percentage of nanofillers induces a weakened interphase as the number of bonded polymers is reduced owing to the decreased polymer fraction, which decreases the mechanical performance (III in Fig. 4d). The strong interfacial interaction induced by the critical interphase was confirmed by the relatively neat fracture with rare pull-out of CNTs and a dense fracture surface (Fig. 4e and Extended Data Fig. 6). In addition, the large aspect ratio of GO nanosheets leads to better stress transfer and higher cohesive strength, and the well-dispersed CNTs can further enhance the reinforcing effect by strengthening the mechanical properties of the polymer matrix and bridging adjacent nanosheets. All these together result in the record high tensile strength and modulus compared with the reported nanocomposite films prepared by traditional strategies, including layer-by-layer (LBL), casting and vacuum filtration (Fig. 4f and Supplementary Table 7).

Employing this superspreading layering strategy, we also fabricated nanoclay-based (SS-clay/CNT) nanocomposite films with enhanced toughness, as this material property is important for practical applications<sup>35</sup>. The toughness of the SS-clay/CNT nanocomposite films reaches a value of  $36.7 \pm 3.0$  MJ m<sup>-3</sup>, which is 20.4 times higher than that of natural nacre; meanwhile, their tensile strength was as high as  $1,195 \pm 60$  MPa (Fig. 4g, Supplementary Figs. 19 and 20, and Supplementary Tables 7 and 8). The enhancement mechanism is similar to that of the SS-GO/clay/CNT nanocomposite films (Supplementary Figs. 20 and 21, and Supplementary Table 5). The critical interphase dramatically resists the formation and propagation of cracks under high tensile stress. The small aspect ratio of clay nanosheets allows a transition of the deformation mode from nanosheet fracture to nanosheet pull-out<sup>10</sup>. The wavy line fracture surface and the pull-out of CNTs (Fig. 4h and Extended Data Fig. 7) lead to the pronounced inelastic deformation and contribute to the efficient dissipation of fracture energy. The above effects synergistically improved the strength and toughness of the SS-clay/CNT nanocomposite films simultaneously.

Bulk nacre-mimetic materials, which are important for practical applications<sup>29</sup>, are challenging to fabricate straightforwardly. Here, we produced a bulk artificial nacre (4 cm × 4 cm × 0.2 cm) by simply laminating the SS-GO/clay/CNT nanocomposite films (Fig. 4i). Under the same impact force, natural mussel nacre cracked into pieces, while the bulk artificial nacre maintained its integrity with just an indentation left on its surface (Fig. 4j). The tensile test results show that the bulk artificial nacre has a modulus similar to natural nacre. Its strength and toughness are about 4 and 2 times greater, respectively, than those of natural nacre (Supplementary Fig. 22 and Supplementary Table 9).

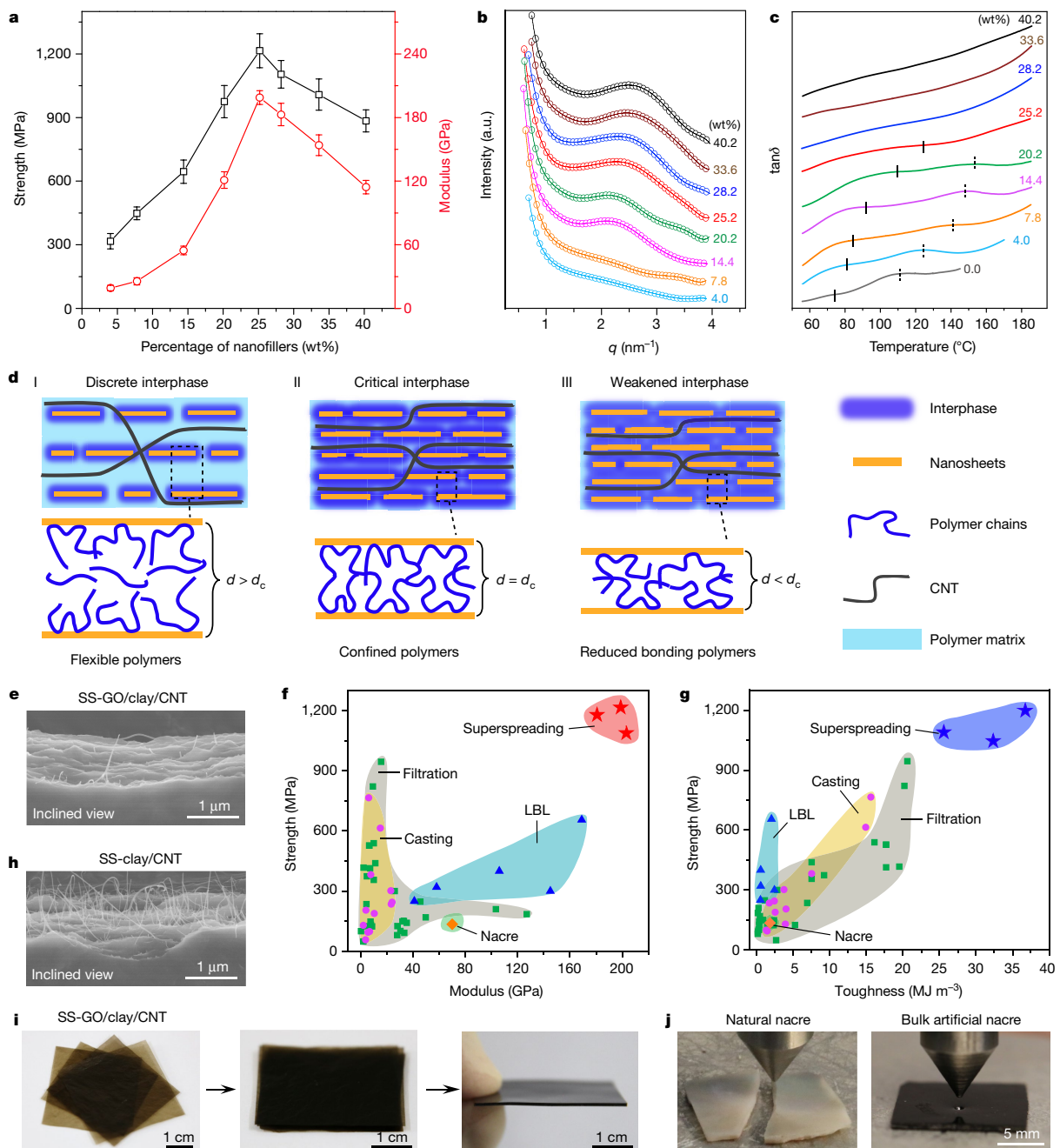


**Fig. 4 | Materials characterization of the layered nanocomposite films.** **a–c**, The strength and modulus (**a**), plots of diffraction vector ( $q$ ) (**b**) and curves of  $\tan\delta$  versus temperature (**c**) of nanocomposite films with various weight percentages of nanofillers (GO, clay and CNTs). The constitution of all the reaction solutions, the detailed mechanical properties data and the corresponding interlayer distance are listed in Extended Data Table 1. Error bars,  $\pm 1$  s.d. In **b** and **c** the curves for each sample have been vertically shifted for clarity.  $\delta$  is the lag angle and  $\tan\delta$  is the loss factor in the dynamic mechanical analysis. The  $T_g$  of each sample was obtained from the  $\tan\delta$ . **d**, Schematic diagram illustrating the interphase between the aligned nanosheets at different interlayer distances,  $d$ . **e**, Inclined view of the fracture surface of the SS-GO/clay/CNT nanocomposite film. The relatively neat fracture with rare pull-out of CNTs and a dense fracture surface illustrate strong interactions between nanofillers and polymers. **f**, Comparison of strength and modulus of

the SS-GO/clay/CNT nanocomposite films prepared by the superspreading strategy, LBL, casting and filtration processes; the corresponding properties of natural nacre are also shown. **g**, Comparison of strength and toughness of the SS-clay/CNT nanocomposite films prepared by the superspreading strategy, LBL, casting and filtration processes; the corresponding properties of natural nacre are also shown. **h**, Inclined view of the fracture surface of the SS-clay/CNT nanocomposite film. The relatively dense fracture surface indicates that the strong interfacial interactions between layered structures of nanosheets and the pull-out of CNTs are due to the high toughness. **i**, The fabrication of bulk artificial nacre using our layered nanocomposite films by a simple laminating process. **j**, Photographs of mussel nacre and bulk artificial nacre under the same impact force (160 N), illustrating the higher impact resistance of the bulk artificial nacre.

We have presented a generalizable and scalable layering method based on the superspreading shear-flow-induced alignment of nanosheets at an immiscible hydrogel/oil interface, and have shown that it is straightforward to fabricate layered nanocomposite films

from a wide range of polymers and 2D nanofillers. We foresee further broadening of the use of this superspreading layering strategy in the development of advanced layered nanocomposites for practical applications.

## Online content

Any methods, additional references, Nature Research reporting summaries, source data, extended data, supplementary information, acknowledgements, peer review information; details of author contributions and competing interests; and statements of data and code availability are available at <https://doi.org/10.1038/s41586-020-2161-8>.

1. Mayer, G. Rigid biological systems as models for synthetic composites. *Science* **310**, 1144–1147 (2005).
2. Meyers, M. A., McKittrick, J. & Chen, P. Structural biological materials: critical mechanics-materials connections. *Science* **339**, 773–779 (2013).
3. Wegst, U. G. K., Bai, H., Saiz, E., Tomsia, A. P. & Ritchie, R. O. Bioinspired structural materials. *Nat. Mater.* **14**, 23–36 (2015).
4. Podsiadlo, P. et al. Ultrastrong and stiff layered polymer nanocomposites. *Science* **318**, 80–83 (2007).
5. Munch, E. et al. Tough, bio-inspired hybrid materials. *Science* **322**, 1516–1520 (2008).
6. Mao, L. et al. Synthetic nacre by predesigned matrix-directed mineralization. *Science* **354**, 107–110 (2016).
7. Tang, Z., Kotov, N. A., Magonov, S. & Ozturk, B. Nanostructured artificial nacre. *Nat. Mater.* **2**, 413–418 (2003).
8. Richardson, J. J., Björnalm, M. & Caruso, F. Technology-driven layer-by-layer assembly of nanofilms. *Science* **348**, aaa2491 (2015).
9. Zhang, M., Huang, L., Chen, J., Li, C. & Shi, G. Ultratough, ultrastrong, and highly conductive graphene films with arbitrary sizes. *Adv. Mater.* **26**, 7588–7592 (2014).
10. Das, P. et al. Nacre-mimetics with synthetic nanoclays up to ultrahigh aspect ratios. *Nat. Commun.* **6**, 5967 (2015).
11. Walther, A. et al. Large-area, lightweight and thick biomimetic composites with superior material properties via fast, economic, and green pathways. *Nano Lett.* **10**, 2742–2748 (2010).
12. Putz, K. W., Compton, O. C., Palmeri, M. J., Nguyen, S. T. & Brinson, L. C. High-nanofiller-content graphene oxide-polymer nanocomposites via vacuum-assisted self-assembly. *Adv. Funct. Mater.* **20**, 3322–3329 (2010).
13. Dikin, D. A. et al. Preparation and characterization of graphene oxide paper. *Nature* **448**, 457–460 (2007).
14. Erb, R. M., Libanori, R., Rothfuchs, N. & Studart, A. R. Composites reinforced in three dimensions by using low magnetic fields. *Science* **335**, 199–204 (2012).
15. Liu, M. et al. An anisotropic hydrogel with electrostatic repulsion between cofacially aligned nanosheets. *Nature* **517**, 68–72 (2015).
16. Guell, D. & Bénard, A. *Flow-Induced Alignment in Composite Materials* (eds Papathanasiou, T. D. & Guell, D. C.) Ch. 1, 1–42 (Woodhead Publishing, 1997).
17. Ding, F. et al. Biomimetic nanocoatings with exceptional mechanical, barrier, and flame-retardant properties from large-scale one-step coassembly. *Sci. Adv.* **3**, e1701212 (2017).
18. Yu, X., Prevot, M. S., Guijarro, N. & Sivula, K. Self-assembled 2D WS<sub>2</sub> thin films for photoelectrochemical hydrogen production. *Nat. Commun.* **6**, 7596 (2015).
19. Zhang, P. et al. Superspreading on immersed gel surfaces for the confined synthesis of thin polymer films. *Angew. Chem. Int. Ed.* **55**, 3615–3619 (2016).
20. Zhao, C. et al. Superspreading-based fabrication of asymmetric porous PAA-g-PVDF membranes for efficient water flow gating. *Adv. Mater. Interfaces* **3**, 1600615 (2016).
21. Hao, Q. et al. Confined synthesis of two-dimensional covalent organic framework thin films within superspreading water layer. *J. Am. Chem. Soc.* **140**, 12152–12158 (2018).
22. de Gennes, P.-G., Brochard-Wyart, F. & Quéré, D. *Capillarity and Wetting Phenomena* (Springer, 2004).
23. Wu, L. et al. Magnetically induced anisotropic orientation of graphene oxide locked by in situ hydrogelation. *ACS Nano* **8**, 4640–4649 (2014).
24. Zerda, A. S. & Lesser, A. J. Intercalated clay nanocomposites: morphology, mechanics, and fracture behavior. *J. Polym. Sci. B* **39**, 1137–1146 (2001).
25. Pavlidou, S. & Papaspyrides, C. D. A review on polymer-layered silicate nanocomposites. *Prog. Polym. Sci.* **33**, 1119–1198 (2008).
26. Genix, A. C. et al. Understanding the static interfacial polymer layer by exploring the dispersion states of nanocomposites. *ACS Appl. Mater. Interfaces* **11**, 17863–17872 (2019).
27. An, Z., Compton, O. C., Putz, K. W., Brinson, L. C. & Nguyen, S. B. T. Bio-inspired borate cross-linking in ultra-stiff graphene oxide thin films. *Adv. Mater.* **23**, 3842–3846 (2011).
28. Zhu, J., Zhang, H. & Kotov, N. A. Thermodynamic and structural insights into nanocomposites engineering by comparing two materials assembly techniques for graphene. *ACS Nano* **7**, 4818–4829 (2013).
29. Kinloch, I. A., Suhr, J., Lou, J., Young, R. J. & Ajayan, P. M. Composites with carbon nanotubes and graphene: an outlook. *Science* **362**, 547–553 (2018).
30. Wen, Y., Wu, M., Zhang, M., Li, C. & Shi, G. Topological design of ultrastrong and highly conductive graphene films. *Adv. Mater.* **29**, 1702831 (2017).
31. Xiong, R. et al. Ultrarobust transparent cellulose nanocrystal-graphene membranes with high electrical conductivity. *Adv. Mater.* **28**, 1501–1509 (2016).
32. Hu, K., Gupta, M. K., Kulkarni, D. D. & Tsukruk, V. V. Ultra-robust graphene oxide-silk fibroin nanocomposite membranes. *Adv. Mater.* **25**, 2301–2307 (2013).
33. Ramanathan, T. et al. Functionalized graphene sheets for polymer nanocomposites. *Nat. Nanotechnol.* **3**, 327–331 (2008).
34. Bansal, A. et al. Quantitative equivalence between polymer nanocomposites and thin polymer films. *Nat. Mater.* **4**, 693–698 (2005).
35. Ritchie, R. O. The conflicts between strength and toughness. *Nat. Mater.* **10**, 817–822 (2011).

**Publisher's note** Springer Nature remains neutral with regard to jurisdictional claims in published maps and institutional affiliations.

© The Author(s), under exclusive licence to Springer Nature Limited 2020

## Methods

### Preparation of PAAm hydrogels

An aqueous solution of acrylamide (15 g), *N,N'*-methylenebis(acrylamide) (0.3 g) and ammonium persulphate (0.3 g) in 100 ml of distilled water was prepared. The PAAm hydrogel was synthesized by radical polymerization for 5 min after the addition of *N,N,N',N'*-Tetramethylethylenediamine (300  $\mu$ l) to 100 ml of the above solution at room temperature. Then the obtained hydrogels were rinsed in abundant water to wash off the unreacted components and make sure the hydrogels were fully swollen.

### Synthesis of CA hydrogels

The CA hydrogel was fabricated on a cleaned glass surface by spin-coating it with a sodium alginate (NaAlg) solution (2 w/v%) that was subsequently gelled in a  $\text{CaCl}_2$  solution (1 M). Then the obtained hydrogels were rinsed in abundant water to wash off the unreacted components and make sure the hydrogels were fully swollen.

### Preparation of reaction solutions

Before preparing the reaction solutions, we first made stock solutions for the polymers (NaAlg and PVA) and nanofillers (GO, clay and CNTs). NaAlg powder was dissolved in deionized water and stirred overnight to obtain a NaAlg solution (2 wt%). A GO dispersion was further diluted in deionized water, stirred for 2 h, and then subjected to ultrasound for 30 min to obtain the GO solution (0.1 wt%). Clay nanosheets were dispersed in deionized water and stirred overnight to obtain a transparent clay nanosheets solution (2 wt%). PVA powder was dissolved in water at 80 °C under slow stirring to form an aqueous solution (4 wt%). The CNT dispersion (0.1 wt%) was used as received. Then, the above stock solutions were added to deionized water in order (that is, PVA solution, NaAlg solution and then the nanosheets dispersion) to prepare various reaction solutions with different weight percentages of polymers and nanofillers. The mixed solution was sonicated for 10 min with 100 W power to obtain homogenous reaction solutions. Specifically, for the reaction solutions containing CNTs, CNT dispersion was added before all other components.

### Preparing layered nanocomposite films

Before the fabrication process, the prepared fully swollen hydrogels were placed into an equal weight of deionized water. Then  $\text{CaCl}_2$  powder was added into the mixture, and the final concentration of  $\text{CaCl}_2$  was 0.05 M (solution B). After soaking for 30 min, the hydrogels containing  $\text{Ca}^{2+}$  ions were obtained. The obtained PVA solution, NaAlg solution, GO solution, clay solution and water were successively added to a beaker in different ratios and then stirred and subjected to ultrasound for a few minutes to obtain the homogenous reaction solution. During the fabricating process, the prepared reaction solution was continuously extruded from an array of syringes with needles (15G) onto an oil-immersed hydrogel surface. Upon contacting the hydrogel surface, the dropped reaction solution superspreads, enabling us to obtain a stable and homogeneous liquid layer at the oil and hydrogel interface. By regulating the flow rate of the reaction solution and the distance between adjacent syringes, these multiple sources of reaction solution from different syringes were able to spread and coalesce together, forming a uniform solution layer on the hydrogel surface (the hydrogel had been previously immersed in a  $\text{CaCl}_2$  solution moving at a constant speed). The reaction solution layer gelatinized into a gel rapidly by *in situ* ionic crosslinking of NaAlg as  $\text{Ca}^{2+}$  ions diffused from the hydrogel surface to the liquid film during the spreading process. This gel film could be readily separated from the hydrogel surface in a water bath. After drying the gel films in a drying oven at 60 °C and at atmospheric pressure for 5 h, uniform and continuous nanocomposite films without defects can be collected as a roll.

For the preparation of SS-GO/agarose nanocomposite films, 1 g agarose powder was dissolved in 100 ml deionized water at 90 °C and

stirred for 8 h to obtain an agarose solution (1 wt%). 10 ml GO dispersion (0.1 wt%) was gradually added to the agarose solution by stirring at 90 °C. The obtained homogenous solution was rapidly extruded from an array of syringes with needles (15G) onto an oil-immersed PAAm hydrogel surface. The reaction solution layer gelatinized into a GO/agarose gel film rapidly by gelation of agarose as the temperature dropped. This gel film could be readily separated from the hydrogel surface in a water bath. After drying the gel films in a drying oven at 60 °C for 24 h, uniform and continuous SS-GO/agarose nanocomposite films without defects can be obtained.

For the preparation of SS-GO/PAAm nanocomposite films, an aqueous solution mixture of acrylamide (30 g), *N,N'*-methylenebis(acrylamide) (0.6 g) and photoinitiator 2959 (0.6 g) in 100 ml distilled water was prepared. 200 ml GO (0.1 wt%) dispersion was gradually added to the prepared solution with stirring for 2 h. The obtained homogenous reaction solutions were extruded from an array of syringes with needles (15G) onto an oil-immersed CA hydrogel surface. After irradiation under a high-pressure mercury arc lamp (Perfectlight 100 W) for 100 s, the GO/PAAm gel film was synthesized. This gel film could be readily separated from the CA hydrogel surface in a water bath. After drying the GO/acrylamide gel films in a drying oven at 60 °C for 24 h, uniform and continuous SS-GO/PAAm nanocomposite films without defects were obtained.

### Preparation of the PS-GO/CA films

The homogenous solution containing NaAlg and nanofillers was drop-wise placed onto the surface of hydrogel that had been soaked in the  $\text{CaCl}_2$  solution at ambient conditions (room temperature and 40–50% relative humidity) as depicted in Supplementary Fig. 7. After the reaction completed within 20 min, the PS gel was formed and could be easily separated from the hydrogel surface in a water bath. The free-standing gel film that floated on the water's surface was transferred to a Teflon film and was further dried in a drying oven at 60 °C for more than 3 h. The dried PS film can be easily detached from the Teflon films and then set aside for further characterization.

### Fabrication of bulk artificial materials

To fabricate bulk artificial materials, the prepared SS-GO/clay/CNT nanocomposite films were cut into pieces of equal sizes and spray-coated with a thin layer of PVA solution on the surface. They were then laminated together by stacking and were pre-pressed at 1 MPa at 60 °C for 24 h. A second hot-pressing step with 10 MPa was applied at 60 °C for another 24 h.

### Mechanical tests of nanocomposite films

Stress-strain curves were obtained by testing rectangular strips of the layered nanocomposite films (3 mm width and 10 mm length) with a mechanical strength tester ESM301 from Mark-10 Corporation. Tests were performed at a rate of 1 mm min<sup>-1</sup>. The mechanical properties for each sample are based on the average value of 8–10 specimens. The specimens were first dried in an oven at 60 °C at atmospheric pressure for 5 h, and then were equilibrated at a condition of 25 °C and 10% relative humidity for 48 h before mechanical testing. The thickness of all samples was calculated by SEM. The Young's modulus of all samples was determined by the slope of the linear region of the stress-strain curves.

### Instruments and characterization

The spreading processes were recorded by using a high-speed camera (i-SPEED 3, Olympus) at room temperature. The solution characterization was carried out at 25 °C by using an Anton Paar model MCR-302 rheometer in a range of 1–100 rad s<sup>-1</sup>. The morphology of the obtained films was characterized by scanning electron microscopy (SEM; JEOL SU8010 operated at 5 kV). Atomic force microscopy (AFM) images were obtained using a Bruker Multimode 8, operated in tapping mode at a scan rate of 1 Hz. Transmission electron microscopy (TEM) images were obtained using an HT7700 instrument at 100 kV.

Small-angle X-ray scattering (SAXS) was carried out at BL45XU in SPring-8 (Hyogo, Japan)<sup>36</sup> with a Rigaku imaging plate area detector model R-AXIS IV++. The scattering vector  $\mathbf{q}$  (where  $q = 4\pi \sin\theta/\lambda$ ;  $2\theta$  and  $\lambda$  were the scattering angle and wavelength of an incident X-ray beam (1.00 Å), respectively) and the position of an incident X-ray beam on the detector were calibrated using several orders of layer reflections from silver behenate ( $d = 58.380$  Å). The sample-to-detector distance was 28 cm. The recorded scattering/diffraction images were integrated along the Debye–Scherrer ring using Rigaku model R-AXIS Display software, affording a one-dimensional scattering profile. The SAXS results in Fig. 4b, Extended Data Figs. 4 and 5 and Supplementary Fig. 20 were obtained on a Xenocs Xeuss SAXS/WAXS System using Cu-K $\alpha$  radiation. The distance between the sample and the detector was 42.3 cm. Optical microscopic imaging of the reaction solutions with different concentrations of nanofillers was performed using a Nikon model Eclipse LV100NPOL apparatus. The reaction solutions were observed between two glass slides. The dynamic mechanical analysis was performed on a TA Q800 DMA (TA Instruments). The measurements were carried out at a frequency of 1 Hz and an amplitude of 0.05% strain. The  $\tan\delta$  values were obtained with a temperature ramp of 5 °C min<sup>-1</sup>.

### Estimation of the orientation order

The orientation order parameter ( $f$ ) was estimated using the azimuthal angle plots obtained from the 2D SAXS images<sup>37,38</sup>. The  $f$  values range between 0 and 1, where the former corresponds to an isotropic structure, and the latter corresponds to perfect orientation along the director. A Maier–Saupe distribution function was used to fit the azimuthal angle plots<sup>37</sup>:

$$I = I_0 + A \exp[\omega \cos^2(\varphi - \varphi_0)]$$

where  $I_0$  denotes the free baseline intensity,  $\varphi_0$  is the azimuth at the position of the maximal intensity,  $\varphi$  is the azimuth and  $\omega$  is the parameter that determines the width of the distribution. After the curve fitting of this function to the azimuthal angle plot, parameters  $I_0$ ,  $A$  and  $\omega$  were obtained. The orientation order parameter  $f$  was determined using the following equation<sup>38</sup>:

$$f = \frac{\int_{-1}^1 P_2(\cos\varphi) \exp(\omega \cos^2 \varphi) d(\cos\varphi)}{\int_{-1}^1 \exp(\omega \cos^2 \varphi) d(\cos\varphi)}$$

where the function  $P_2(\cos\varphi)$  is the second-order Legendre polynomial of  $\cos\varphi$ , often referred to as the Hermans orientation function,

$$P_2(\cos\varphi) = \frac{1}{2}(3\cos^2\varphi - 1)$$

### Spreading of a single droplet

To elucidate the essence of the shear-flow-induced alignment of nanosheets in the superspreading process, we analyse the spreading dynamics of one single droplet on a gel surface (Extended Data Fig. 1a). Assuming cylindrical asymmetry, the velocity profile inside the droplet is given by  $v(r, z; t)$ . When the droplet height  $H$  is much smaller than its radius  $R$ , we can assume that the droplet has a parabolic shape  $h(r, t) = H(t) \left[1 - \frac{r^2}{R(t)^2}\right]$ , and the velocity is along the radial direction. Here  $h$  is the droplet height at position  $r$ . The total volume of the droplet is given by  $V_0 = (\pi/2)H(t)R(t)^2$ . The height-average flow velocity  $\bar{v}(r) = \int_h^0 v(r, z) dz/h$  satisfies the volume conservation equation  $\frac{d}{dt} \int_r^0 dr' 2\pi r' h(r', t) = -2\pi r \bar{v}(r, t) h(r, t)$ . Combined with the total volume, we obtain the height-average velocity  $\bar{v}(r, t) = (r/R)\dot{R}$ , where  $\dot{R}$  is the velocity of the contact line.

The velocity along the  $z$  direction has a parabolic profile. The boundary condition at the substrate is  $v(r, z=0; t)=0$ . Near the interface, the

no-slip boundary condition can also be applied because the viscosity of the surrounding fluid is much larger than that of the droplet liquid. Therefore, the velocity takes the form  $v(z, r; t) = -A(r)z^2 + A(r)hz$ , with  $A(r) = \frac{6r}{h^2} \frac{R}{R}$ . The velocity near the contact line is larger than that near the centre, and the shear rate  $\partial v / \partial z$  is also larger near the contact line. The high shear rate produced by the superspreading is responsible for the alignment of the nanosheets.

The dynamics of droplet spreading can be calculated using the Onsager principle<sup>39</sup>. The free energy of the droplet is given by  $F = \gamma_{OL}\pi(R^2 + H^2) + (\gamma_{LG} - \gamma_{OG})\pi R^2 = (\gamma_{OL} + \gamma_{LG} - \gamma_{OG})\pi R^2 + \gamma_{OL}\frac{4V_0^2}{\pi R^4}$ , where  $\gamma_{OL}$  is the oil/liquid interfacial tension,  $\pi(R^2 + H^2)$  is the interfacial area between the oil and the droplet,  $\gamma_{LG}$  and  $\gamma_{OG}$  are the interfacial tension between liquid/gel and oil/gel, and  $\pi R^2$  is the interfacial area between the droplet and gel substrate. When the droplet is large, the contribution due to the  $R^{-4}$  term is small and can be neglected. It is also reasonable to assume that interfacial tension between the droplet and the hydrogel vanishes ( $\gamma_{LG} = 0$ ) because the hydrogel is swollen by the same liquid of the droplet. The change rate of the free energy is then given by  $\dot{F} \approx (\gamma_{OL} - \gamma_{OG})2\pi R \dot{R} = -\Delta\gamma 2\pi R \dot{R}$ , with  $\Delta\gamma = \gamma_{OG} - \gamma_{OL}$ .

The dissipation function has two parts. One is the viscous dissipation inside the droplet. Using the lubrication approximation, the viscous dissipation function is  $\Phi_s = \frac{1}{2} \int_R^\infty \frac{12\eta}{h} \dot{v}^2 2\pi r dr = \frac{3\pi^2 \eta \ell}{V_0} R^4 \dot{R}^2$ . The integral diverges at  $r \rightarrow R$ , which can be resolved by truncating the integral at  $r \rightarrow R - a$  ( $a$  being the molecular size). This leads to a dimensionless coefficient  $\ell$ , which has a numerical value ranging from<sup>22</sup> 15 to 20. The second contribution to the dissipation function is due to the contact line friction  $\Phi_{cl} = \frac{1}{2} \xi_{cl} (2\pi R) \dot{R}^2$ , where  $\xi_{cl}$  is a phenomenological parameter characterizing the friction constant of the moving contact line<sup>40</sup>.

The dynamics of the droplet spreading is then given by the Onsager variational principle  $\partial(\dot{F} + \Phi)/\partial\dot{R} = 0$ . This leads to  $\dot{R} = \Delta\gamma / \left( \frac{3\pi\eta\ell}{V_0} R^3 + \xi_{cl} \right)$ , with the solution  $\frac{3\pi\eta\ell}{4V_0} R^4 + \xi_{cl} R = \Delta\gamma t$ . The dynamics can be separated into two regions. When  $R$  is small, the  $\xi_{cl}$  term dominates, leading to a constant spreading speed, that is,  $R \propto t$ . When  $R$  is large, the  $R^4$  term prevails, and the spreading follows the scaling  $R \propto t^{1/4}$ . We measured the droplet radius as a function of time for various solutions with different viscosity. The results (symbols represent our experimental results) are plotted in a log–log plot (Extended Data Fig. 2a). The straight lines show the initial  $t^1$  scaling and later  $t^{1/4}$  scaling.

Note that it is crucially important for superspreading that  $\Delta\gamma$  be positive. This is possible because the spreading takes place on a gel surface. For a hard surface, a microscopic precursor film develops ahead of the macroscopic droplet (Extended Data Fig. 1b). In this case  $\Delta\gamma = \gamma_{OL} - \gamma_{LG} = 0$ . One then has to consider the next leading term in the free energy, which is  $\gamma_{OL}\frac{4V_0^2}{\pi R^4}$ . This leads to Tanner's law of spreading with  $R \propto t^{1/10}$  scaling<sup>41</sup>, which is a much slower process than  $t^{1/4}$ . In our experiments, the gel is soft, and the gel surface is slightly elevated near the contact line (Extended Data Fig. 1c). This prevents the formation of the precursor film. Owing to the presence of the polymer component, the interfacial tension between gel/oil might be larger than the interfacial tension between liquid/oil, that is,  $\Delta\gamma = \gamma_{OG} - \gamma_{OL} > 0$ . This difference in the interfacial tension provides the driving force for the superspreading.

### Spreading on a moving substrate

We now consider the spreading of a liquid on a moving substrate. In the frame of the substrate, the spreading takes place in a quasi-two-dimensional case. If  $Q$  is the flow rate and  $V$  is the moving speed of a substrate, the liquid has a constant area  $A_0 = Q/V$  in the plane perpendicular to the moving direction of the substrate. This is the controlling parameter that we can vary either by changing the flow rate or the moving speed of the substrate.

The evolution equation can be derived following similar procedures for the droplet case. The results are  $\dot{R} = \Delta\gamma / \left( \frac{16\eta\ell}{A_0} R^2 + \xi_{cl} \right)$  and

# Article

$\frac{16\eta\ell}{3A_0}R^3 + \xi_{cl}R = \Delta\gamma t$ . The dynamics can also be separated into two regions. When  $R$  is small, the  $\xi_{cl}$  term dominates, leading to a constant spreading speed, that is,  $R \propto t$ . This is the same as in the droplet case. When  $R$  is large, the  $R^3$  term prevails, and the spreading follows  $R \propto t^{1/3}$ . This is slightly different than the droplet case ( $R \propto t^{1/4}$ ). The experimental measurement is shown in Extended Data Fig. 2b, showing the two regions with different scaling.

The final spreading diameter  $d$  can be calculated when the spreading speed reduces to a small value  $v_{small}$ . The square of the spreading diameter is  $d^2 = 4R^2|_{R=v_{small}} = \left(\frac{\Delta\gamma}{v_{small}} - \xi_{cl}\right)\frac{A_0}{16\eta\ell} = \left(\frac{\Delta\gamma}{v_{small}} - \xi_{cl}\right)\frac{1}{16\eta\ell}\frac{Q}{V}$ . Thus, the diameter scales with the flow rate as  $d \propto Q^{1/2}$ , and varies with the substrate speed as  $d \propto V^{-1/2}$ . To increase the spreading diameter, one can either increase the flow rate or reduce the moving speed of the hydrogel substrate. The spreading diameter can also be tuned by changing the solution viscosity: the solution with lower viscosity spreads faster.

For a typical fabrication process, the measured spreading diameters value  $d$  as a function of flow rate  $Q$  can be fitted well by  $d \propto Q^{1/2}$ , as shown as the red line in Fig. 2a. The measured spreading diameters as functions of the substrate speed  $V$  and the solvent viscosity  $\eta$  are shown in Extended Data Fig. 3.

## Separation in syringe arrays

The distance between adjacent syringes has to be carefully chosen such that the final film will be uniform. When the distance  $L$  was equal to the spreading diameter  $d$ , we observed continuous but non-uniform films due to the lack of spreading force at the edge of the solution layers, preventing them from coalescing. This can be understood from the levelling of a horizontal film.

Initially when the edges of the solution layers come together, the film is non-uniform. The main driving force for the levelling is the interfacial tension. The levelling dynamics can be characterized by a timescale  $\tau_{level}$ , which is roughly the time required for the non-uniform film to become uniform. This time is given by<sup>22</sup>  $\tau_{level} \approx \eta\lambda^4 / (\gamma_{OL}e_0^3)$ , where  $\lambda$  is the characteristic length of non-uniformity and  $e_0$  is the averaged thickness of the film. For a typical operation time  $\tau_{level} \approx 10$  s,  $\eta = 5.5$  mPa s,  $\gamma_{OL} = 37$  mN m<sup>-1</sup>,  $e_0 = 0.4$  mm, one obtains  $\lambda \approx 8$  mm. Thus, for the non-uniformity with a characteristic length larger than 8 mm, it takes longer than 10 s for the film to level. The optimal syringe separation would be less than  $d$  but larger than  $d - 8$  mm. In our experiments, it was found that the optimal separation is  $d - 6$  mm.

## Estimation of timescales

The flow-induced alignment of plate-like particles is the result of competition between two processes. One is the shear flow; one plate particle experiences different speeds in the direction perpendicular to the shear-flow direction. Shear flow is the driving force for the alignment. The timescale associated with the alignment is given by the reciprocal of shear rate,  $1/\dot{\gamma}$ . In a flow with shear rate  $\dot{\gamma}$ , it takes about time  $\tau_{shear} = 1/\dot{\gamma}$  for the plates to be aligned in the direction of flow. In our experiments, we can estimate the shear rate by  $\dot{\gamma} = v/e_0$ , where  $v$  is the average flow velocity and  $e_0$  is the film thickness. For typical numbers  $v = 0.2$  m s<sup>-1</sup> and  $e_0 = 0.4$  mm, we get  $\tau_{shear} = 1/\dot{\gamma} \approx 0.002$  s. The other process is the rotational diffusion of the particle, characterized by the rotational diffusion constant  $D_R$ . The rotational diffusion will cause the plate to take the random direction, and this is the counterforce to the alignment. The rotational diffusion time is of the order of  $\tau_{rotation} = (2\pi)^2/D_R$ . The rotational diffusion constant for a particle of size  $a$  is given by  $D_R = k_B T / (6\pi\eta a^3)$ . For graphene oxide (GO) of the size

$a \approx 1$  μm and room temperature  $k_B T = 4.14 \times 10^{-21}$  J, we get  $D_R = 0.04$  s<sup>-1</sup> and  $\tau_{rotation} \approx 1,000$  s.

When the condition  $\tau_{rotation} > \tau_{shear}$  is satisfied, the shear flow dominates the rotational diffusion, and the plate particles can be aligned by the shear flow. In the opposite case  $\tau_{rotation} < \tau_{shear}$ , rotational diffusion is the faster process. Even when plates are initially aligned, the alignment is quickly destroyed by the fast rotation. In our experiments,  $\tau_{rotation} \gg \tau_{shear}$ , therefore the shear flow can effectively align the GO sheets. We can also calculate the particle size  $a^*$  that leads to  $\tau_{rotation} = \tau_{shear}$ . For the shear rate in our experiments, this corresponds to  $a^* = 12$  nm. Therefore, our superspreading shear flow can effectively align nanosheets of size larger than 12 nm. Smaller particles are more difficult to align.

Another important timescale is the gelation time. In our experiments, we fix the transiently ordered structure via the ionic crosslinking of NaAlg by Ca<sup>2+</sup>. The associated timescale is the time required for Ca<sup>2+</sup> ions to diffuse from the hydrogel surface to the solution. For typical diffusion constant  $D = 10^{-9}$  m<sup>2</sup> s<sup>-1</sup> and film thickness  $e_0 = 0.4$  mm, we can estimate the gelation time  $\tau_{gelation} \approx e_0^2/D \approx 160$  s. The gelation time has to be larger than the timescale  $\tau_{level} \approx 10$  s for film levelling; otherwise non-uniform film would be fixed by the gelation. This timescale also has to be smaller than the rotational diffusion time  $\tau_{rotation} \approx 1,000$  s; otherwise the good alignment produced by superspreading is not maintained.

In our superspreading method, the relevant timescales should satisfy the relation  $\tau_{shear}$  (0.002 s) <  $\tau_{level}$  (10 s) <  $\tau_{gelation}$  (160 s) <  $\tau_{rotation}$  (1,000 s). Typical experimental values are shown in parentheses.

## Data availability

The data that support the findings of this study are available from the corresponding author on reasonable request.

36. Fujisawa, T. et al. Small-angle X-ray scattering station at the SPring-8 RIKEN beamline. *J. Appl. Crystallogr.* **33**, 797–800 (2000).
37. Feng, S. et al. Hierarchical structure in oriented fibers of a dendronized polymer. *Macromolecules* **42**, 281–287 (2009).
38. Nie, Y. et al. New insights into thermodynamic description of strain-induced crystallization of peroxide cross-linked natural rubber filled with clay by tube model. *Polymer* **52**, 3234–3242 (2011).
39. Doi, M. *Soft Matter Physics* (Oxford Univ. Press, 2013).
40. Man, X. & Doi, M. Ring to mountain transition in deposition pattern of drying droplets. *Phys. Rev. Lett.* **116**, 066101 (2016).
41. Tanner, L. H. The spreading of silicone oil drops on horizontal surfaces. *J. Phys. D* **12**, 1473–1484 (1979).

**Acknowledgements** This research was supported by the National Key R&D Program of China (2017YFA0207800), the National Natural Science Funds for Distinguished Young Scholars (21725401), the National Natural Science Foundation (21988102, 21774004), the 111 project (B14009) and the Fundamental Research Funds for the Central Universities. The small-angle X-ray scattering measurements were performed at BL45XU in SPring-8 with the approval of the RIKEN SPring-8 Center (proposal 20180067).

**Author contributions** C.Z., P.Z. and J.Z. contributed equally to this work. L.J. and M.L. contributed to the initiating idea. C.Z. performed the experiments. R.S. contributed to the fabrication of nanocomposite films and mechanical tests. J.Z. contributed to the theoretical analysis of the spreading liquid. Y.I. and Y.Y. supported the X-ray diffraction measurements at SPring-8. S.Q., R.F., S.W., A.P.T. and L.J. contributed to the analysis of mechanical properties. C.Z., P.Z., J.Z. and M.L. analysed all the data and wrote the manuscript. All authors commented on the manuscript.

**Competing interests** The authors declare no competing interests.

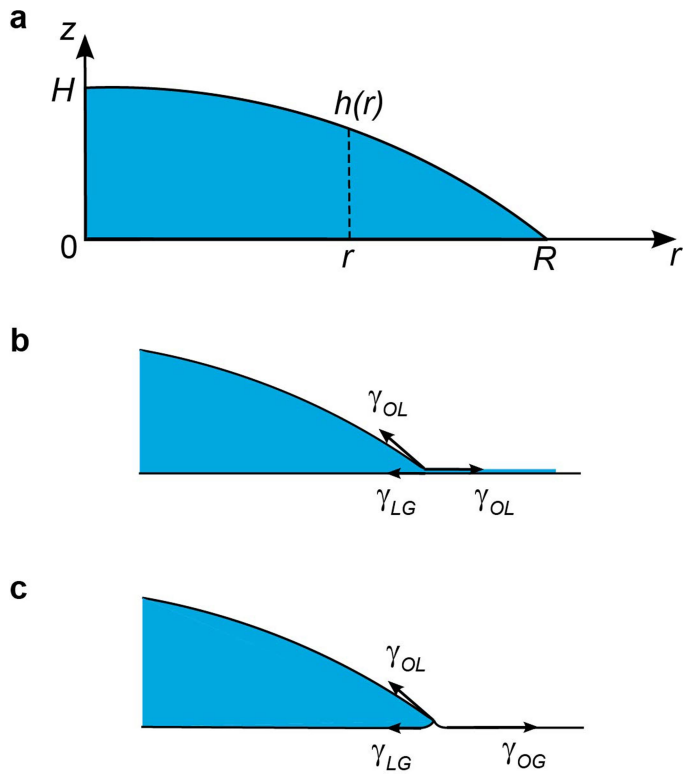
## Additional information

**Supplementary information** is available for this paper at <https://doi.org/10.1038/s41586-020-2161-8>.

**Correspondence and requests for materials** should be addressed to M.L.

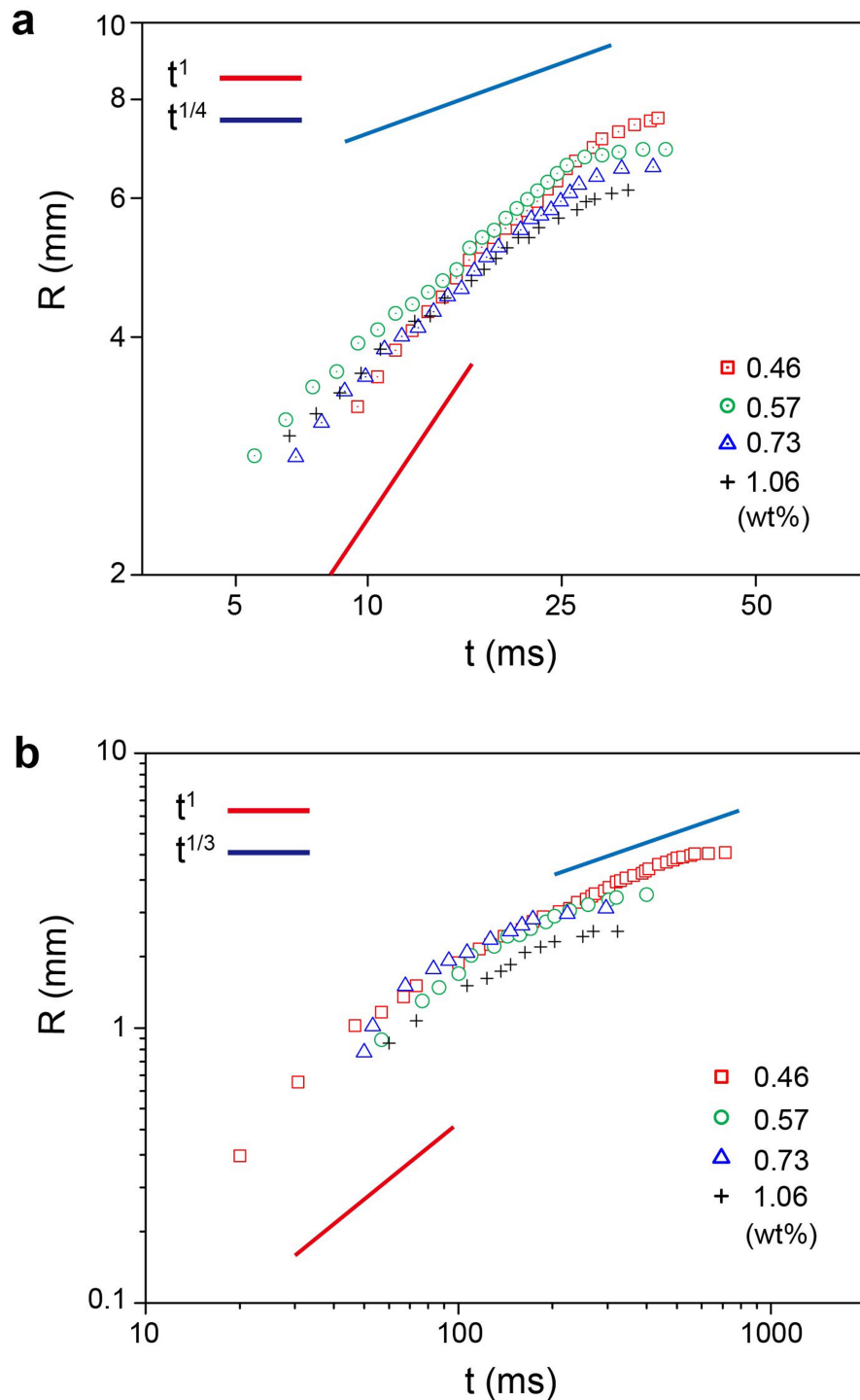
**Peer review information** *Nature* thanks André Studart, Hongbin Lu and Karl W. Putz for their contribution to the peer review of this work.

**Reprints and permissions information** is available at <http://www.nature.com/reprints>.



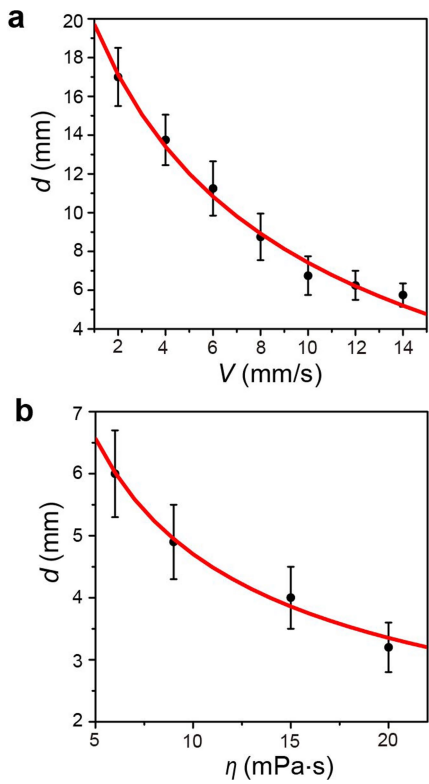
**Extended Data Fig. 1 | Schematic pictures of a spreading droplet.**

**a**, Coordinate system of the spreading process for a single droplet. **b**, Spreading on a solid wetting surface. **c**, Spreading on a soft gel surface. See Methods for nomenclature.

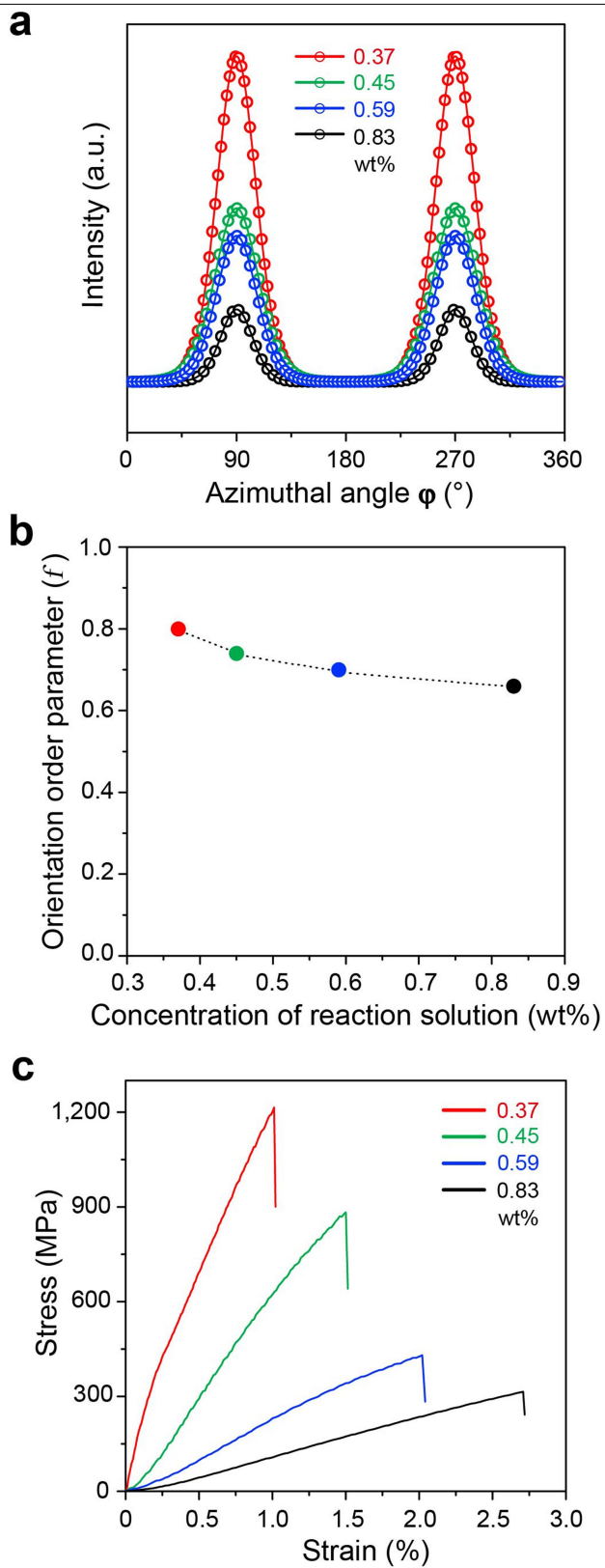


**Extended Data Fig. 2 | The spreading radius of reaction solutions with different concentrations as a function of time.** **a**, The spreading radius ( $R$ ) of a single droplet as a function of time ( $t$ ) for various spreading solutions with different concentrations. The time evolution of the radius shows a transition from  $t^1$  (red line) to  $t^{1/4}$  (blue line) scaling. **b**, The spreading radius  $R$  of various

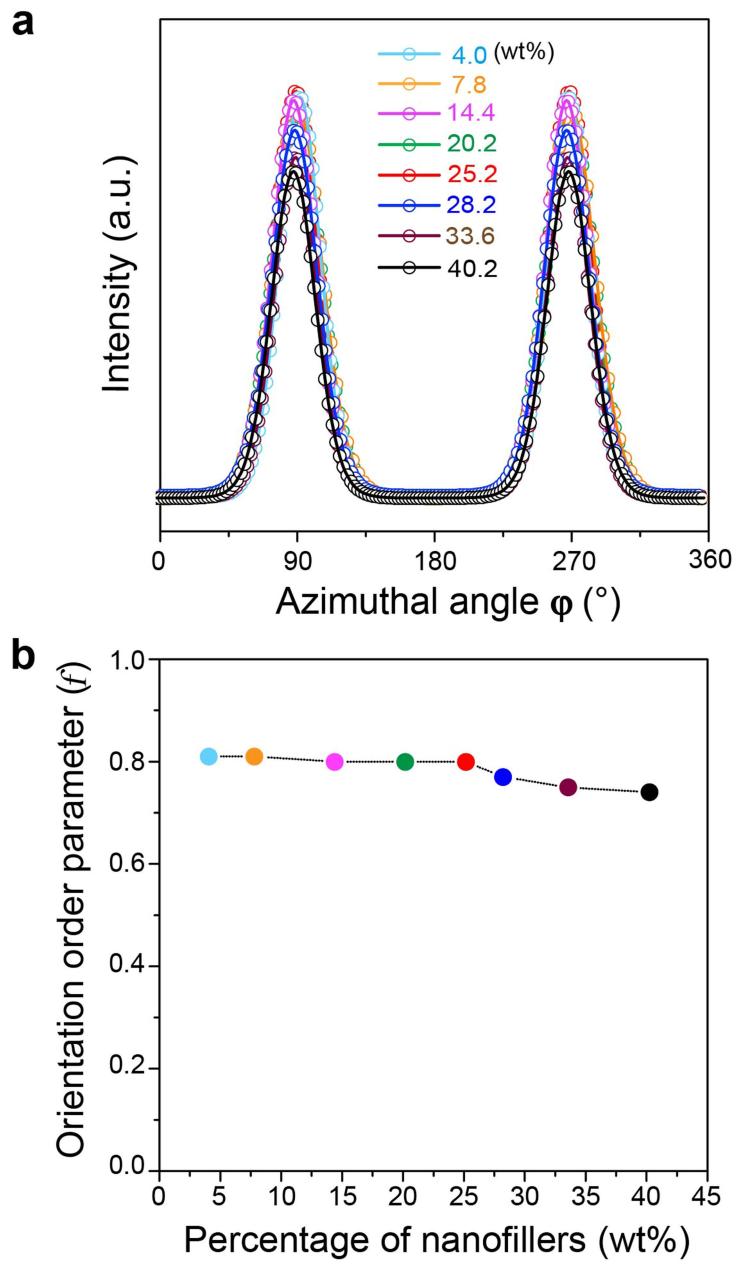
spreading solutions with different concentrations on a moving substrate as a function of time. The time evolution of the radius shows a transition from  $t^1$  (red line) to  $t^{1/3}$  (blue line) scaling. For **a** and **b** the compositions of the four kinds of reaction solutions are listed in Supplementary Table 5 (the reaction solutions for the resulting clay/CNT-based nanocomposite films).



**Extended Data Fig. 3 | Factors affecting the spreading diameter  $d$ .** **a**, The spreading diameter  $d$  as a function of the moving speed of the hydrogel substrate  $V$  for a given reaction solution with a viscosity of 6 mPa s. The flow rate  $Q$  was 70 ml h<sup>-1</sup>. The composition of the reaction solution is 0.03 wt% GO and 0.15 wt% NaAlg. **b**, The spreading diameter  $d$  as a function of the viscosity of the reaction solutions  $\eta$ . The moving speed of the hydrogel substrate  $V$  was 5 mm s<sup>-1</sup> and the flow rate  $Q$  was 70 ml h<sup>-1</sup>. The viscosity of the aqueous solution was changed by altering the concentration of NaAlg and GO nanosheets. Red lines, fitting curves; error bars,  $\pm 1$ s.d.

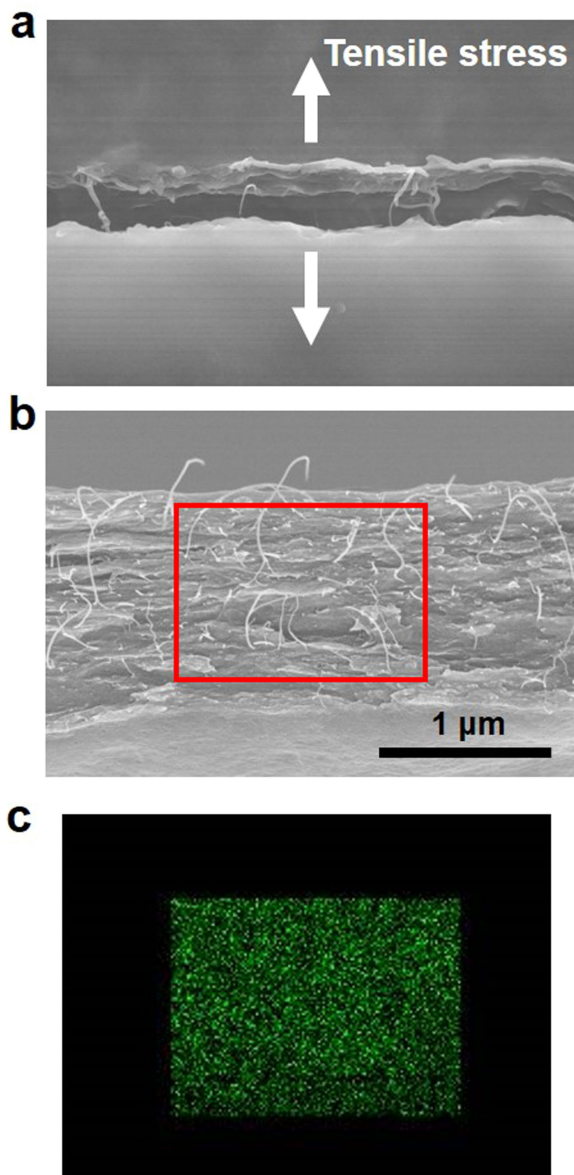


**Extended Data Fig. 4 | The influence of the concentration of the reaction solution on the orientation degree and on the mechanical properties of the GO/clay/CNT-based nanocomposite films.** **a–c**, Plots of azimuthal angle ( $\varphi$ ; **a**), orientation order parameter ( $f$ ) versus concentration (**b**), and stress–strain curves (**c**) of the prepared GO/clay/CNT-based nanocomposite films, using reaction solutions with different concentrations of nanofillers (in wt%, see key). The constitution of the four kinds of reaction solutions, the detailed orientation order parameter ( $f$ ), and the detailed mechanical properties data are listed in Supplementary Tables 5 and 6.

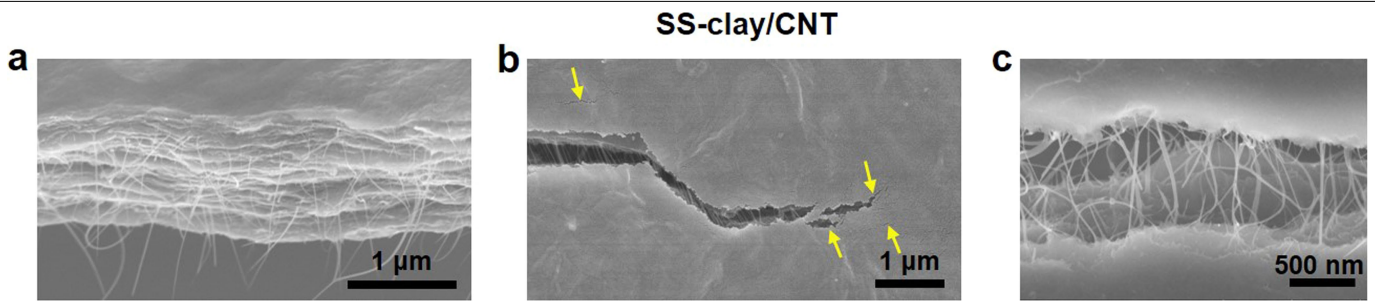


**Extended Data Fig. 5 | Structural characterization of the layered nanocomposite films with various weight percentages of nanofillers (GO, clay and CNTs).** **a, b,** Plots of azimuthal angle  $\varphi$  (**a**) and the orientation order parameter ( $f$ ) of the layered nanocomposite films with different weight

percentages of nanofillers prepared by the superspreading strategy (see key). These results confirm that nanosheets were assembled into highly ordered structures in all these films. The constitution of the reaction solutions and the detailed orientation order parameter ( $f$ ) are listed in Extended Data Table 1.



**Extended Data Fig. 6 | Fracture behaviour of the SS-GO/clay/CNT nanocomposite films.** **a**, A failure crack propagates almost in a straight line and perpendicular to the tensile stress direction. **b**, The morphology of the cross-section view of the fracture surface. CNTs were rarely pulled out from the relatively neat fracture surface, indicating the strong interactions between nanofillers and polymers. **c**, The energy dispersive X-ray spectroscopy (EDS) image of Si originating from clay in the SS-GO/clay/CNT nanocomposite films, revealing the even distribution of clay nanosheets. The scale bar in SEM image **b** applies also to SEM image **a** and EDS image **c**.



**Extended Data Fig. 7 | Fracture behaviour of the SS-clay/CNT nanocomposite films.**

**a**, The morphology of the cross-section view of the fracture surface.

**b**, The crack path shows a wavy line parallel to the crack propagation path and a damaged zone around the propagating crack tip (indicated by yellow arrows),

indicating the efficient dissipation of fracture energy. **c**, At a higher magnification, the pull-out of CNTs further contributes to fracture energy dissipation. **a–c** are SEM images.

# Article

**Extended Data Table 1 | Summary of results**

Nanofillers (wt%)	3250 mg aqueous solution		Strength (MPa)	Modulus (GPa)	Ultimate strain (%)	Toughness (MJ/m <sup>3</sup> )	Orientation order parameter ( <i>f</i> )	Interlayer distance <i>d</i> (nm)
	(m <sub>NaAlg</sub> , m <sub>PVA</sub> , m <sub>GO</sub> , m <sub>clay</sub> , m <sub>CNT</sub> ) mg							
4.0	(5, 4, 0.125, 0.25, 0.004)		317 ± 36	19.2 ± 2.6	2.4 ± 0.2	3.2 ± 0.6	0.81	/
7.8	(5, 4, 0.25, 0.5, 0.008)		448 ± 30	25.6 ± 3.4	2.0 ± 0.2	4.9 ± 0.6	0.81	/
14.4	(5, 4, 0.5, 1, 0.015)		645 ± 55	54.7 ± 4.1	1.6 ± 0.2	6.3 ± 0.5	0.80	3.08
20.2	(5, 4, 0.75, 1.5, 0.023)		975 ± 76	121.1 ± 7.8	1.2 ± 0.1	6.4 ± 0.5	0.80	2.98
25.2	(5, 4, 1, 2, 0.03)		1215 ± 80	198.8 ± 6.5	1.0 ± 0.1	6.9 ± 0.4	0.80	2.62
28.2	(5, 4, 1.25, 2.5, 0.038)		1104 ± 65	182.9 ± 10.6	1.0 ± 0.08	5.9 ± 0.3	0.77	2.59
33.6	(5, 4, 1.5, 3, 0.045)		1008 ± 74	153.9 ± 9.7	0.98 ± 0.06	5.2 ± 0.2	0.75	2.56
40.2	(5, 4, 2, 4, 0.06)		884 ± 52	114.4 ± 6.4	0.96 ± 0.05	4.6 ± 0.2	0.74	2.51

Summary of the composition of the reaction solution, the mechanical properties and the SAXS results for nanocomposite films with various weight percentages of nanofillers (GO, clay and CNTs). The data shown are mean ± s.d.